

ROBUST TRAJECTORY DESIGN FOR RENDEZVOUS IN A NEAR RECTILINEAR HALO ORBIT

Timothy Goulet*, David Woffinden†, Nathan Collins‡, Blythe Andrews§

Future NASA Artemis missions will require complex docking plans between the Orion capsule and Lunar Gateway that meet predetermined safety constraints while minimizing fuel usage and state uncertainty at rendezvous. In this paper, linear covariance analysis is applied to a first order relative form of Near-Rectilinear Halo Orbit dynamics to determine the nominal trajectories and state dispersions associated with various maneuver profiles in the Sun-referenced Local Vertical Local Horizontal reference frame of the lunar Gateway. These maneuver profiles are optimized using a particle swarm optimizer and direct search algorithm to find trajectories that satisfy approach corridor, free drift, velocity magnitude, underburn, and maneuver transfer time safety constraints to 3σ certainty.

INTRODUCTION

The execution of rendezvous, proximity operations, and docking (RPOD) in an Earth-Moon Near Rectilinear Halo Orbit (NRHO)^{1,2} is becoming an integral component to the NASA programs pushing for lunar exploration and beyond. Current plans include the development of a lunar Gateway vehicle that remains in an NRHO, a subset of the halo orbit family characterized by close passage over one of the lunar poles. As illustrated in Figure 1, the NRHO proposed for future Gateway missions is a seven-day period southern NRHO, which reaches its furthest distance from the Moon over the lunar south pole. The vision for Gateway is a crew-tended, cislunar haven to be used as a staging point to support lunar surface missions and travel to Mars. With so much importance given to a single spacecraft, RPOD activities with Gateway will prove crucial to mission success for some of NASA's most high-profile missions. Although the ability to successfully perform RPOD has been the cornerstone of human space exploration since its inception, the new flight regime in an NRHO poses unique challenges.

This work begins investigating the process of optimizing rendezvous trajectory profiles in an NRHO that account for the complex interaction of the overall integrated guidance, navigation, and control (GN&C) system performance while minimizing the relative trajectory dispersions and total 3σ Δv usage. Relative navigation accuracy, translational burn placement, maneuver execution errors, relative targeting algorithms, disturbance accelerations, and initial state uncertainties are all integrated into the optimization process. The inclusion of the system uncertainty in the trajectory design process is referred to as robust trajectory optimization or robust trajectory design.

Previous efforts have utilized convex optimization techniques to develop and analyze far-field rendezvous reference trajectories in an NRHO accounting for an assortment of constraints, but did not include uncertainties in the system⁸ when optimizing the profile. The use of robust trajectory design has since been developed and demonstrated for rendezvous in low Earth orbit.³ It was then extended to cislunar outbound trajectories to an NRHO⁴ and introduced for a simple rendezvous approach trajectory in the NRHO⁵ for mid-course correction placement. Recently, these robust trajectory optimization principles have been applied to solve lunar powered descent and landing⁶ along with Mars aerocapture⁷ problems. The objective of this research is to

*Cadet, Department of Astronautics, United States Air Force Academy, USAF Academy, CO, 80840

†Aerospace Engineer, GN&C Autonomous Flight Systems Branch, NASA Johnson Space Center, Houston TX, 77058

‡Assistant Professor of Astronautics, Department of Astronautics, United States Air Force Academy, USAF Academy, CO, 80840

§Assistant Professor of Astronautics, Department of Astronautics, United States Air Force Academy, USAF Academy, CO, 80840

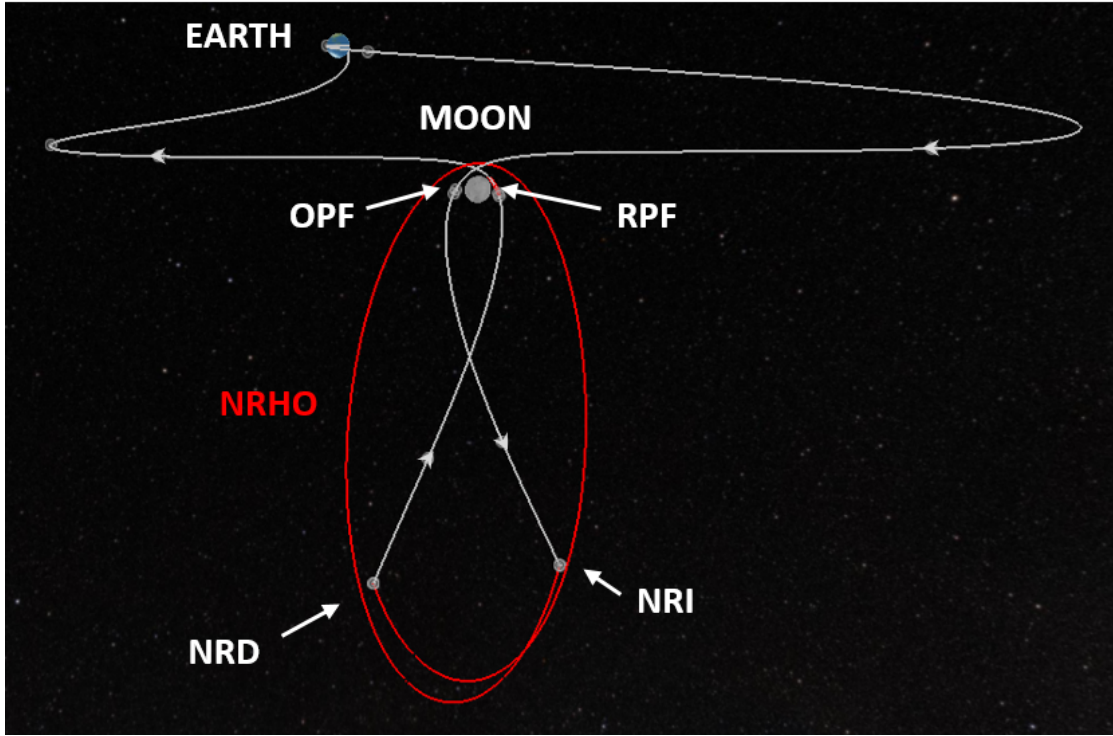


Figure 1. Notional Orion Artemis III Trajectory to a Southern Near Rectilinear Halo Orbit (NRHO).

demonstrate robust trajectory design for rendezvous in an NRHO and identify optimal maneuver profiles for different rendezvous duration and initiation distances.

ANALYSIS APPROACH

Performance Metrics

Several performance metrics are utilized to optimize the performance of an NRHO rendezvous profile with system uncertainty. These include the true trajectory dispersions $\delta \mathbf{x}$, the navigation dispersions $\delta \hat{\mathbf{x}}$, the true navigation error $\delta \mathbf{e}$, and the onboard navigation error $\delta \hat{\mathbf{e}}$ as depicted in Figure 2. The true dispersions $\delta \mathbf{x}$ are defined as the difference between the true state \mathbf{x} and the nominal state $\bar{\mathbf{x}}$. The true state \mathbf{x} is an n -dimensional vector that represents the *real world* environment or actual state.

$$\delta \mathbf{x} \triangleq \mathbf{x} - \bar{\mathbf{x}} \quad \mathbf{D} = E [\delta \mathbf{x} \delta \mathbf{x}^T] \quad (1)$$

The nominal state $\bar{\mathbf{x}}$ is also an n -dimensional vector that represents the desired or reference state. The covariance of the environment dispersions, \mathbf{D} , indicates how precisely a GN&C system can follow a desired trajectory.

The navigation dispersions $\delta \hat{\mathbf{x}}$ are defined as the difference between the navigation state $\hat{\mathbf{x}}$ and the nominal state $\bar{\mathbf{x}}$. The navigation state is an \hat{n} -dimensional vector ($\hat{n} < n$) that represents the filter's estimated state.

$$\delta \hat{\mathbf{x}} \triangleq \hat{\mathbf{x}} - \mathbf{M}_x \bar{\mathbf{x}} \quad \hat{\mathbf{D}} = E [\delta \hat{\mathbf{x}} \delta \hat{\mathbf{x}}^T] \quad (2)$$

The matrix \mathbf{M}_x is an $(\hat{n} \times n)$ matrix that maps the estimated state in terms of the true and nominal state. The covariance of the navigation dispersions, $\hat{\mathbf{D}}$, reflect how precisely the onboard system thinks it can follow a prescribed reference trajectory.

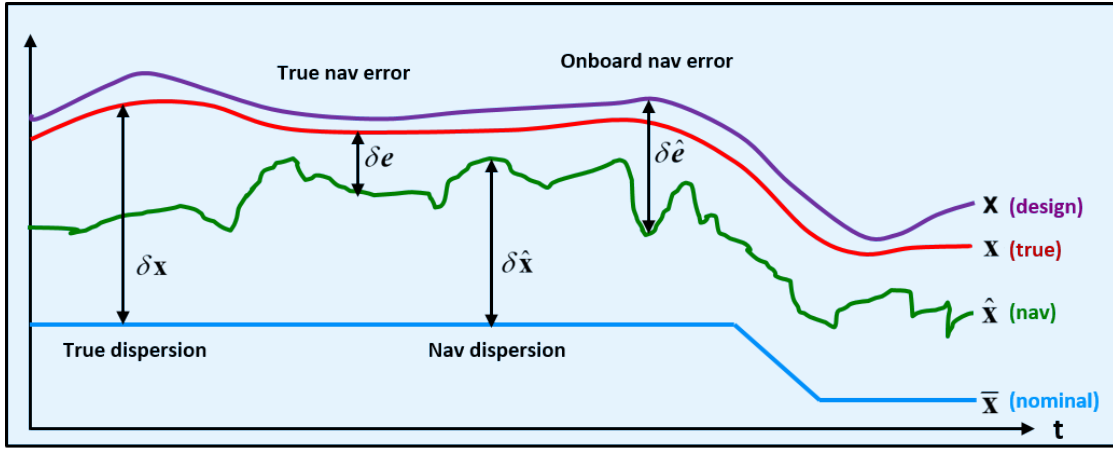


Figure 2. GN&C Performance Metric Variables

The true navigation error $\delta \mathbf{e}$ is the difference between the environment and navigation states. It is also the difference between the environment and the navigation dispersions.

$$\delta \mathbf{e} \triangleq \mathbf{M}_x \mathbf{x} - \hat{\mathbf{x}} = \mathbf{M}_x \delta \mathbf{x} - \delta \hat{\mathbf{x}} \quad \mathbf{P} = E [\delta \mathbf{e} \delta \mathbf{e}^T] \quad (3)$$

The covariance of the true navigation error, \mathbf{P} , quantifies how precisely the onboard navigation system can estimate the actual state.

The onboard navigation error $\delta \hat{\mathbf{e}}$ itself is never computed, but it is used to develop the onboard navigation filter equations. It is defined as the difference between the design state, \mathbf{x} , and the navigation state $\hat{\mathbf{x}}$.

$$\delta \hat{\mathbf{e}} \triangleq \mathbf{x} - \hat{\mathbf{x}} \quad \hat{\mathbf{P}} = E [\delta \hat{\mathbf{e}} \delta \hat{\mathbf{e}}^T] \quad (4)$$

The covariance of the onboard navigation error, $\hat{\mathbf{P}}$, quantifies how precisely the onboard navigation system expects it can determine the actual state. The performance of the onboard navigation system is determined by comparing $\hat{\mathbf{P}}$ to the actual navigation performance \mathbf{P} . If the *true* states and the *design* states are assumed to be the same, then the true navigation covariance will equal the onboard navigation covariance.

The covariances of the true dispersions, navigation dispersions, true navigation error, and the onboard navigation error are ultimately used to analyze and assess the performance of a proposed GN&C system. A common approach to obtain these performance metrics is to use a Monte Carlo simulation outlined in Figure 3, where the sample statistics of hundreds or thousands of runs, N , are used to numerically compute the desired covariance matrices.

$$\mathbf{D} = \frac{1}{N-1} \sum \delta \mathbf{x} \delta \mathbf{x}^T \quad \hat{\mathbf{D}} = \frac{1}{N-1} \sum \delta \hat{\mathbf{x}} \delta \hat{\mathbf{x}}^T \quad \mathbf{P} = \frac{1}{N-1} \sum \delta \mathbf{e} \delta \mathbf{e}^T \quad (5)$$

The onboard navigation error covariance $\hat{\mathbf{P}}$ is the navigation filter covariance for each run. This same statistical information can be obtained using linear covariance analysis techniques.

Linear covariance analysis incorporates the non-linear system dynamics models and GN&C algorithms to generate a nominal reference trajectory $\bar{\mathbf{x}}$ which is then used to propagate, update, and correct an onboard navigation covariance matrix $\hat{\mathbf{P}}$ and an augmented state covariance matrix \mathbf{C} ,

$$\mathbf{C} = E [\delta \mathbf{X} \delta \mathbf{X}^T] \quad (6)$$

where the augmented state $\delta \mathbf{X}^T = [\delta \mathbf{x}^T \ \delta \hat{\mathbf{x}}^T]$ consists of the true dispersions and the navigation dispersions. Pre- and post-multiplying the augmented state covariance matrix by the following mapping matrices, the

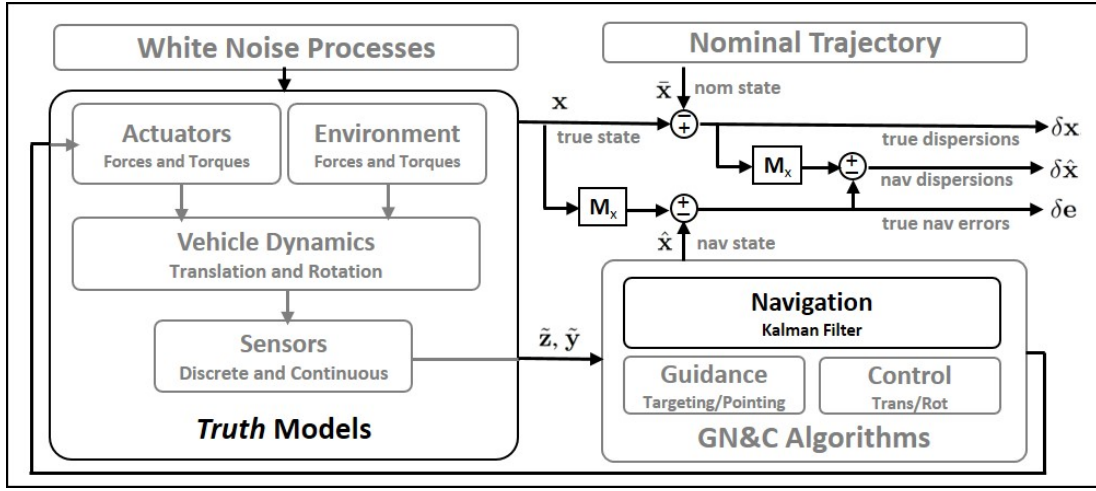


Figure 3. Extracting GN&C Performance Metrics Using Monte Carlo Techniques

covariances for the trajectory dispersions, navigation dispersions, and the navigation error can be obtained.

$$\begin{aligned} \mathbf{D} &= [\mathbf{I}_{n \times n}, \mathbf{0}_{n \times \hat{n}}] \mathbf{C} [\mathbf{I}_{n \times n}, \mathbf{0}_{n \times \hat{n}}]^T \\ \hat{\mathbf{D}} &= [\mathbf{0}_{\hat{n} \times n}, \mathbf{I}_{\hat{n} \times \hat{n}}] \mathbf{C} [\mathbf{0}_{\hat{n} \times n}, \mathbf{I}_{\hat{n} \times \hat{n}}]^T \\ \mathbf{P} &= [\mathbf{I}_{\hat{n} \times n}, -\mathbf{I}_{\hat{n} \times \hat{n}}] \mathbf{C} [\mathbf{I}_{\hat{n} \times n}, -\mathbf{I}_{\hat{n} \times \hat{n}}]^T \end{aligned} \quad (7)$$

Linear Covariance Analysis

The linear covariance (LinCov) analysis equations used to propagate, update, and correct both the augmented state covariance matrix and the onboard navigation covariance matrix are summarized here. For additional details regarding the development and implementation of the linear covariance simulation, see the following references.^{9,10,11,12,13,14}

LinCov Analysis Modeling The discrete-time propagation equations for augmented state covariance matrix \mathbf{C} and the onboard navigation covariance matrix $\hat{\mathbf{P}}$ are

$$\mathbf{C}(t_{k+1}) = \Phi(t_{k+1}, t_k) \mathbf{C}(t_k) \Phi^T(t_{k+1}, t_k) + \mathbf{G} \mathbf{Q} \mathbf{G}^T \quad (8)$$

$$\hat{\mathbf{P}}(t_{k+1}) = \hat{\Phi}(t_{k+1}, t_k) \hat{\mathbf{P}}(t_k) \hat{\Phi}^T(t_{k+1}, t_k) + \hat{\mathbf{G}} \hat{\mathbf{Q}} \hat{\mathbf{G}}^T \quad (9)$$

where Φ and $\hat{\Phi}$ are augmented and onboard state transition matrices respectively for the linearized perturbation dynamics about the reference trajectory. The mapping matrices, \mathbf{G} and $\hat{\mathbf{G}}$, are used to map environmental and navigation process noise characterized by \mathbf{Q} and $\hat{\mathbf{Q}}$, into \mathbf{C} and $\hat{\mathbf{P}}$.

The measurement update equations for augmented and navigation state covariance matrices, \mathbf{C} and $\hat{\mathbf{P}}$, at a measurement time t_i are

$$\mathbf{C}^+(t_i) = \mathbf{A} \mathbf{C}^-(t_i) \mathbf{A}^T + \mathbf{B} \mathbf{R}^j(t_i) \mathbf{B}^T \quad (10)$$

$$\hat{\mathbf{P}}^+(t_i) = [\hat{\mathbf{I}} - \hat{\mathbf{K}}^j(t_i) \hat{\mathbf{H}}^j] \hat{\mathbf{P}}^-(t_i) [I - \hat{\mathbf{K}}^j(t_i) \hat{\mathbf{H}}^j]^T + \hat{\mathbf{K}}^j(t_i) \hat{\mathbf{R}}^j(t_i) \hat{\mathbf{K}}^j(t_i)^T \quad (11)$$

where the superscript ‘j’ denotes the jth measurement type. The Kalman gain is written as

$$\hat{\mathbf{K}}^j(t_i) = \hat{\mathbf{P}}(t_i) (\hat{\mathbf{H}}^j)^T [\hat{\mathbf{H}}^j \hat{\mathbf{P}}^-(t_i) (\hat{\mathbf{H}}^j)^T + \hat{\mathbf{R}}^j(t_i)]^{-1} \quad (12)$$

The matrices $\hat{\mathbf{H}}$ and $\hat{\mathbf{R}}$ are the measurement sensitivity and measurement noise matrices respectively. The matrices \mathbf{A} and \mathbf{B} map the effects of the measurements and their associated noise to the navigation state dispersions.

The correction equations for \mathbf{C} and $\hat{\mathbf{P}}$ at a maneuver time t_m are

$$\mathbf{C}^+(t_m) = \mathbf{M}\mathbf{C}^-(t_m)\mathbf{M}^T + \mathbf{N}\mathbf{Q}_w^{act}\mathbf{N}^T \quad (13)$$

$$\hat{\mathbf{P}}^+(t_m) = [\hat{\mathbf{I}} + \hat{\mathbf{M}}] \hat{\mathbf{P}}^-(t_m) [I + \hat{\mathbf{M}}]^T + \hat{\mathbf{N}}\hat{\mathbf{Q}}_w^{act}\hat{\mathbf{N}}^T \quad (14)$$

The matrices \mathbf{M} and $\hat{\mathbf{M}}$ contain the control partials associated with a linearized two-impulse targeting algorithm. The matrices \mathbf{N} and $\hat{\mathbf{N}}$ are used to map the effects of actuator noise, described by \mathbf{Q}_w^{act} and $\hat{\mathbf{Q}}_w^{act}$, into \mathbf{C} and $\hat{\mathbf{P}}$.

Cost Function Formulation

The presented rendezvous scenario takes four burns to maneuver from NRHO insertion to a predetermined location for translational retrograde burns as the chaser approaches the target spacecraft. In chronological order, these burns are labeled NRHO Insertion (NRI), Maneuver #1 (M1), Maneuver #2 (M2), and Maneuver #3 (M3). Though the NRI burn is part of this scenario, it is performed without relative sensor measurements and thus is excluded from the cost function detailed in Equation 15 below.

The cost function calculates total Δv , which includes nominal fuel usage and 3σ dispersions, across all maneuver burns. Trajectory safety constraints are enforced via large penalties κ added to the cost function when a constraint is violated. This ensures the optimizer prioritizes safety before fuel efficiency. It also creates a discontinuous cost function, which prevents the use of many common optimizers.

$$\text{cost} = \sum_{i=1}^3 (\Delta v(t_i) + 3\sigma_{\Delta v_i}) + \kappa_{\text{approach corridor}} + \kappa_{\text{free drift}} + \kappa_{\text{velocity magnitude}} + \kappa_{\text{underburn}} + \kappa_{\text{transfer time}} \quad (15)$$

The sections below detail the trajectory constraints represented by the κ terms.

Approach Corridor The approach corridor constraint requires nominal trajectories and associated 3σ position dispersions to stay within a $\pm 20^\circ$ cone around the z-axis behind the target vehicle. For this problem, this is due to lighting constraints in the Sun-referenced LVLH coordinate frame. Though the trajectory may begin or end outside of this cone, it must remain within it from 30 minutes prior to the HR1 burn until after the HR3 burn. x-positions are assumed to be negligible for the purpose of determining if the constraint is met.

$$\kappa_{\text{approach corridor}} = \begin{cases} 10000 & \text{if } |\frac{y}{z}| > \tan(20^\circ) \text{ for any } y, z \text{ on the } 3\sigma \text{ position ellipses} \\ 0 & \text{otherwise} \end{cases} \quad (16)$$

Free-Drift The free drift constraint requires that if the thrusters fail after a burn, the nominal state with 3σ dispersions for the associated free-drift trajectories will not encroach a 1 km approach sphere around the target vehicle for the NRI, M1, or M2 burns and a 200 m keep-out-sphere around the target vehicle for the M3 burn.

$$\kappa_{\text{free drift}} = \begin{cases} 10000 & \text{if } \rho - 3\sigma_\rho < \begin{cases} 1000 \text{ m} & \text{for the NRI, M1, or M2 burns} \\ 200 \text{ m} & \text{for the M3 burn} \end{cases} \\ 0 & \text{otherwise} \end{cases} \quad (17)$$

Velocity Magnitude The velocity magnitude constraint requires the magnitude of the velocity vector to monotonically decrease throughout the maneuver profile.

$$\kappa_{\text{velocity magnitude}} = \begin{cases} 10000 & \text{if for some timestep } i, \dot{\rho}_i < \dot{\rho}_{i+1} \\ 0 & \text{otherwise} \end{cases} \quad (18)$$

Underburn The underburn constraint requires the maneuver profile to drift into free space should an underburn occur. This is accomplished by ensuring the free drift component of each burn crosses the y-axis with a negative y-component.

$$\kappa_{\text{underburn}} = \begin{cases} 10000 & \text{if at } z = 0 \text{ for any free drift trajectory, } y \geq 0 \\ 0 & \text{otherwise} \end{cases} \quad (19)$$

Maneuver Transfer Time The maneuver transfer time constraint requires at least one hour between burns. This permits enough time for attitude adjustments and state measurements between maneuvers.

$$\kappa_{\text{transfer time}} = \begin{cases} 10000 & \text{if for burn times } t_i, \min(t_{i+1} - t_i) < 3600\text{sec} \\ 0 & \text{otherwise} \end{cases} \quad (20)$$

Optimization Process

Due to the complex and discontinuous nature of the cost function, the optimization problem is solved using a particle swarm optimizer (PSO) combined with a direct search algorithm. The PSO performs global optimization on the entire search space, with iteration-varying hyperparameters for particle inertia and attraction to local and global minima. These enhance performance by permitting the PSO to initially prioritize exploration of the search space while slowly transitioning to exploitation of the best value found globally. Once the PSO converges, the direct search algorithm continues the optimization process with far fewer cost function evaluations to ensure the optimized solution is at least a local minimum. During each iteration, candidate values of the optimization variables are passed to the LinCov simulation, which passes results into a cost function and then returns the cost value to the optimizer. This process is illustrated in Figure 4.

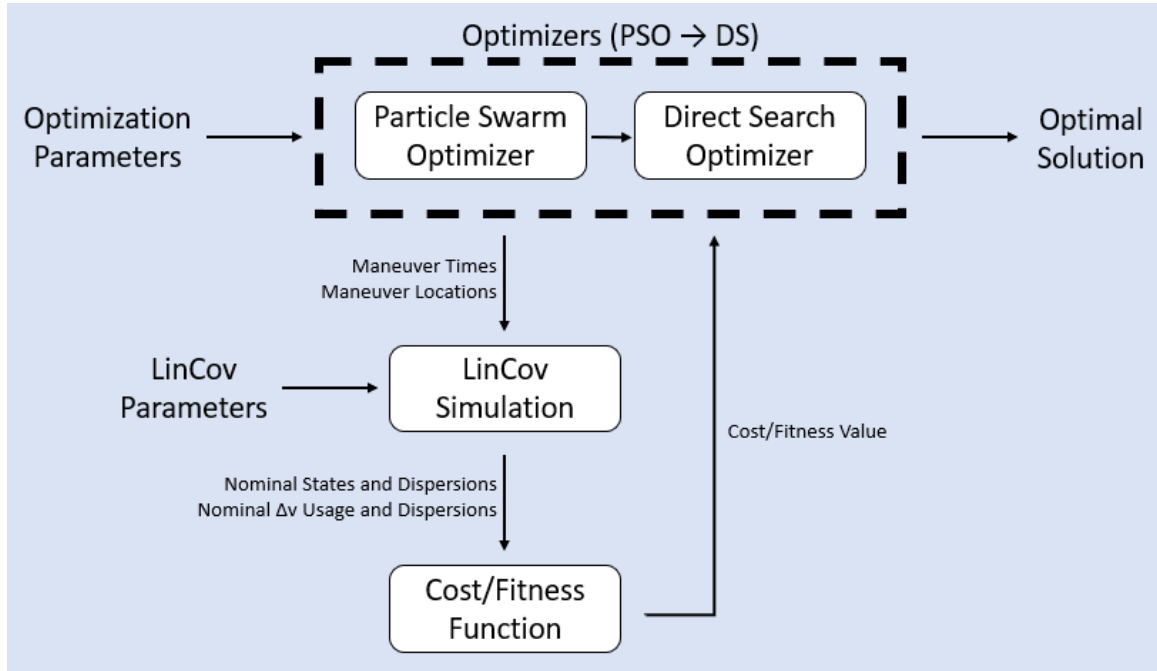


Figure 4. Functional relationship between the LinCov simulation and Optimizers

GN&C RPOD MODELING

Linear Relative Motion

The significant number of calculations made within the optimization process requires a simpler, lower fidelity dynamics model to prevent burdensome computation time. Luquette linearizes relative motion dynamics

for the restricted three body problem (RTBP) about the target spacecraft in his doctoral dissertation *Nonlinear Control Design Techniques for Precision Formation Flying at Lagrange Points*. Assuming the rotation of the Sun-referenced LVLH coordinate frame is negligible, this is expressed as the system of differential equations

$$\dot{\mathbf{X}} = \begin{bmatrix} \mathbf{0}_3 & \mathbf{I}_3 \\ \Xi(t) & \mathbf{0}_3 \end{bmatrix} \mathbf{X} = \mathbf{A}_{LR} \mathbf{X} \quad (21)$$

where

$$\Xi(t) = - \left(\frac{\mu_1}{|\mathbf{r}_{1L}|^3} + \frac{\mu_2}{|\mathbf{r}_{2L}|^3} \right) \mathbf{I}_3 + \frac{3\mu_1}{|\mathbf{r}_{1L}|^3} [\mathbf{e}_{1L} \cdot \mathbf{e}_{1L}^T] + \frac{3\mu_2}{|\mathbf{r}_{2L}|^3} [\mathbf{e}_{2L} \cdot \mathbf{e}_{2L}^T] \quad (22)$$

Figure 5 shows the vectors referenced in Equation 22: \mathbf{r}_{1L} and \mathbf{r}_{2L} refer to the vectors from the two central masses to the leader (target) satellite, whereas \mathbf{e}_{1L} and \mathbf{e}_{2L} refer to the normalized form of these vectors. μ_1 and μ_2 represent the gravitational parameters of the two central masses. In this paper, the two central masses are the Earth and the Moon. Assignment of the "1" and "2" subscripts to these bodies is arbitrary.

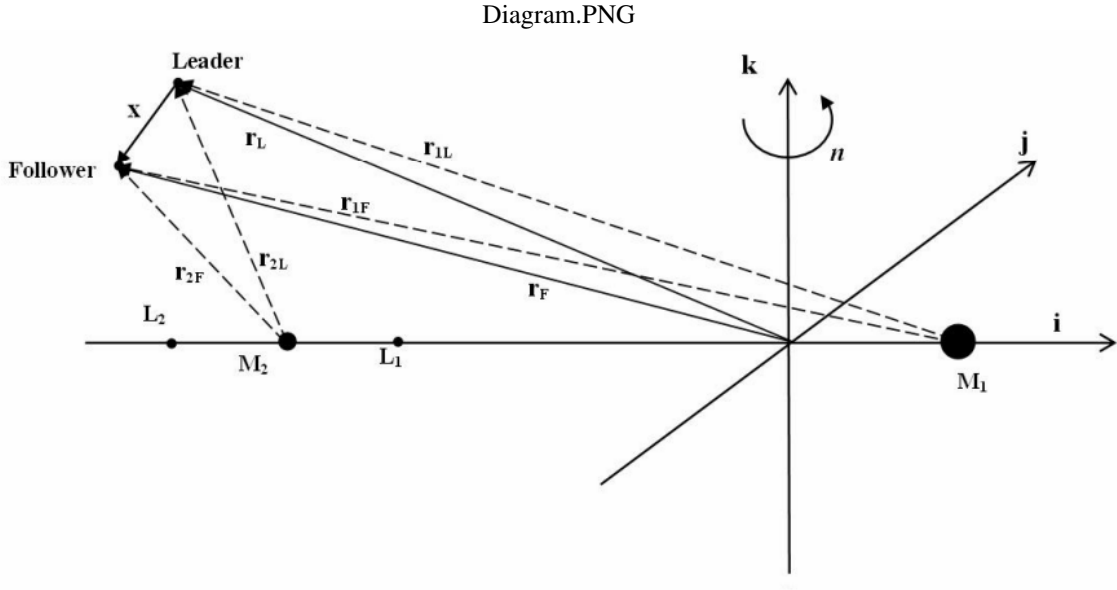


Figure 5. Diagram of vectors in the RTBP

Relative Sensors

Three measurements are taken to aid in navigation state estimation: range, range-rate, and bearing angle. Simplified models are used to represent these sensors to reduce computation time. Mathematical representations are presented in Equations 23-25.

$$\mathbf{z}_\rho = |\mathbf{r}| + \eta_\rho \quad (23)$$

$$\mathbf{z}_{\dot{\rho}} = \mathbf{v}^T \frac{\mathbf{r}}{|\mathbf{r}|} + \eta_{\dot{\rho}} \quad (24)$$

$$\mathbf{z}_{los} = \frac{\mathbf{r}}{|\mathbf{r}|} + \eta_{los} \quad (25)$$

The 3σ dispersions of these measurements are 25 m for range, 0.25 m/s for range-rate, and $2 \cdot 10^{-4}$ rad for bearing angle in all directions.

Relative Targeting

Deriving the targeting equation for linear relative dynamics requires the system's state transition matrix (STM). Though A_{LR} varies with time, this change is negligible for sufficiently small differences in timesteps. For a given time t_j , the system's STM from t_j to $t_j + \Delta t$ is given by

$$\Phi_j(\Delta t) = e^{A_{LR}(t_j)\Delta t} \quad (26)$$

An approximate STM between distant timesteps may be formed via the product of intermediate STMs. Assuming a uniform δt between timesteps such that $\Delta t = n\delta t$,

$$\Phi(\Delta t) = \prod_{j=1}^n \Phi_j(\delta t) \quad (27)$$

Since there are six states in the current system (relative position and velocity vectors), $\Phi(\Delta t)$ is a 6x6 matrix. Thus, it can be broken into four 3x3 components:

$$\Phi(\Delta t) = \begin{bmatrix} \Phi_{rr} & \Phi_{rv} \\ \Phi_{vr} & \Phi_{vv} \end{bmatrix} \quad (28)$$

Using $\Phi(\Delta t)$ to determine how an instantaneous change in velocity $\Delta \mathbf{v}$ will influence the relative position at time $t_i + \Delta t$,

$$\begin{bmatrix} \mathbf{r}_f \\ \mathbf{v}_f \end{bmatrix} = \begin{bmatrix} \Phi_{rr} & \Phi_{rv} \\ \Phi_{vr} & \Phi_{vv} \end{bmatrix} \begin{bmatrix} \mathbf{r}_i \\ \mathbf{v}_i + \Delta \mathbf{v} \end{bmatrix} \quad (29)$$

$$\mathbf{r}_f = \Phi_{rr}\mathbf{r}_i + \Phi_{rv}(\mathbf{v}_i + \Delta \mathbf{v}) \quad (30)$$

So, to target a position \mathbf{r}_f from a given state requires a $\Delta \mathbf{v}$ of

$$\Delta \mathbf{v}_{nominal} = \Phi_{rv}^{-1}(\mathbf{r}_f - \Phi_{rr}\mathbf{r}_i) - \mathbf{v}_i \quad (31)$$

In this simulation, there is 3σ thruster noise of 0.015 m/s. Thus, the actual Δv produced by a maneuver is given by

$$\Delta \mathbf{v}_{actual} = \Delta \mathbf{v}_{nominal} + \eta_{thruster} \quad (32)$$

ROBUST TRAJECTORY DESIGN FOR RENDEZVOUS IN AN NRHO

In total, eight cases will be analyzed with different initiation differences for the NRI burn and initial navigation errors. The rendezvous process from the NRI to M3 burns will take 19,000 seconds in all cases to isolate the effects of modifying these initial conditions. Three different initiation distances for the NRI burn will be analyzed as long, medium, and short profiles. These are presented in Equation 33 below.

$$\mathbf{r}_{long} = \begin{bmatrix} 0 \\ 75 \\ 225 \end{bmatrix} \text{ km}, \quad \mathbf{r}_{medium} = \begin{bmatrix} 0 \\ 50 \\ 175 \end{bmatrix} \text{ km}, \quad \mathbf{r}_{short} = \begin{bmatrix} 0 \\ 25 \\ 125 \end{bmatrix} \text{ km} \quad (33)$$

This analysis assumes initial 3σ state dispersions of 10 km and 0.75 m/s in all directions for position and velocity, respectively, and process noise of $5 \cdot 10^{-8} \text{ m}^2/\text{s}^3$. Two different initial navigation errors are analyzed for each initiation distance as well: a "large" case of 9 km and 0.6 m/s in all directions for position and velocity, respectively, and a "small" case of 5 km and 0.6 m/s in all directions for position and velocity, respectively. These cases are meant to illustrate the benefits of an improved navigation solution on total Δv usage.

Six variables will be optimized to minimize total Δv usage across the three HR burns: y-burn location, z-burn location, and burn time for both the HR1 and HR2 maneuvers. This leaves the optimizer to find the optimal path between the NRI and HR3 burns, signifying the beginning and ending points of the maneuver profile.

Case 0: Unoptimized Trajectory for Long Initiation Distance

Large Navigation Error Beginning with a reasonable but unoptimized trajectory, the proposed maneuver profile meets all trajectory constraints with 22.6709 m/s of total Δv usage between the HR1, HR2, and HR3 burns. Burn locations and ignition times are summarized in Table 1.

Table 1. Baseline maneuver profile for long initiation distance

Burn	Location (km)	Ignition Time (sec)	Total ΔV (m/s)
NRI	$[0, 75, 225]^T$	0	-
HR1	$[0, 25, 125]^T$	8000	9.2872
HR2	$[0, 5, 50]^T$	15500	3.9287
HR3	–	19000	9.4549

The maneuver profile with 3σ position dispersions is presented in Figure 6 below. The shaded region is the 20° approach corridor about each side of the z-axis in the Sun-referenced LVLH coordinate frame.

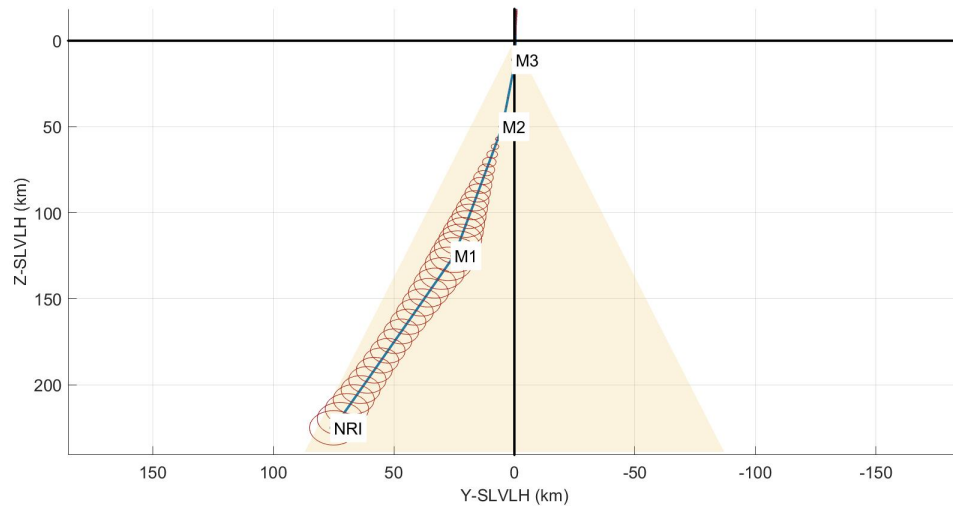


Figure 6. Baseline maneuver profile for long initiation distance with large nav error plotted in the Sun-referenced LVLH frame

The proposed free drift profiles are presented in Figures 7 and 8 below.

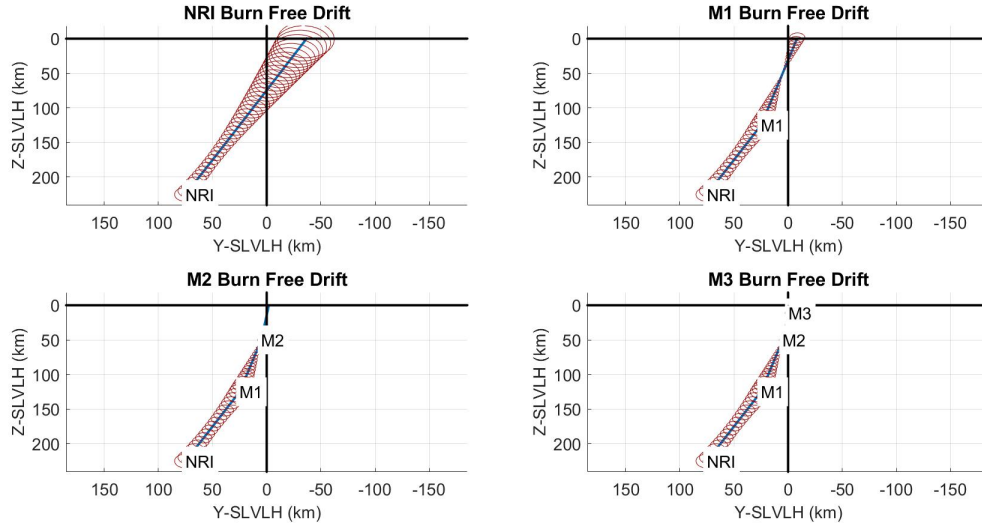


Figure 7. Free-drift trajectories of baseline long maneuver profile with large nav error, zoomed out

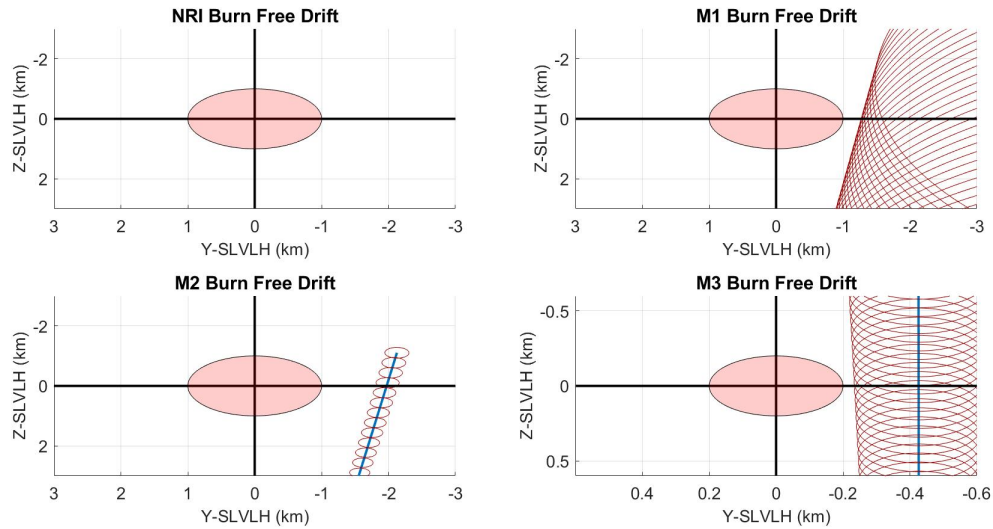


Figure 8. Free-drift trajectories of baseline long maneuver profile with large nav error, zoomed in

There is an inherent tradeoff between position dispersions and Δv usage in this scenario, since burns from further away require subtler changes in angle to the target vehicle at the cost of growing dispersions due to process noise. Thus, this trajectory appears unoptimized due to the noticeable spaces between the 3σ ellipses and approach/keep-out spheres. An optimized trajectory would minimize wasteful maneuvers by positioning initial burns such that the 3σ dispersions hardly miss the approach sphere.

Small Navigation Error Though ignition times and locations do not change with the new initial navigation error, total Δv usage decreases to 20.6518 m/s thanks to the overall reduction in system uncertainty. This is summarized in Table 2.

Table 2. Baseline maneuver profile for long initiation distance with small nav error

Burn	Location (km)	Ignition Time (sec)	Total ΔV (m/s)
NRI	$[0, 75, 225]^T$	0	-
HR1	$[0, 25, 125]^T$	8000	8.0138
HR2	$[0, 5, 50]^T$	15500	3.1830
HR3	–	19000	9.4549

The maneuver profile with 3σ position dispersions is presented in Figure 9 below. Once again, the shaded region is the 20° approach corridor about each side of the z-axis in the Sun-referenced LVLH coordinate frame.

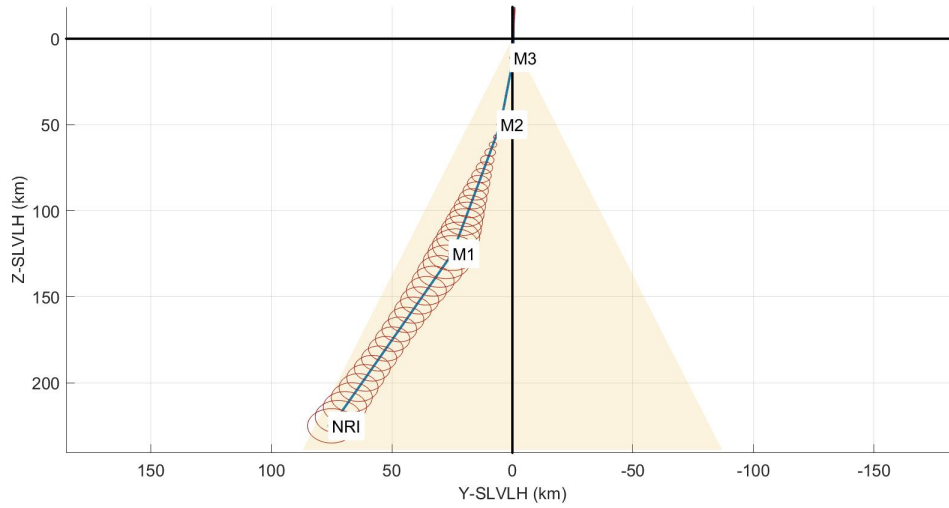


Figure 9. Baseline maneuver profile for long initiation distance with small nav error plotted in the Sun-referenced LVLH frame

The proposed free drift profiles are presented in Figures 10 and 11 below.

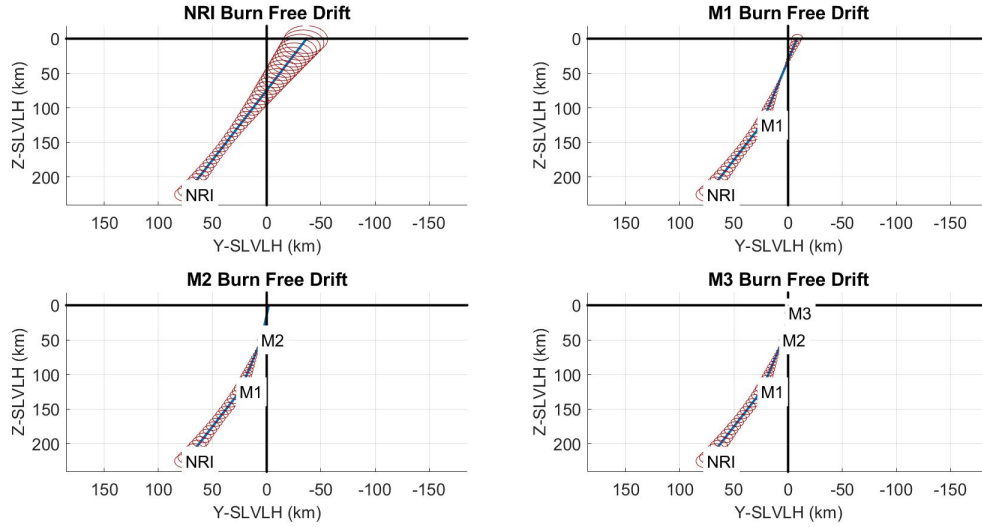


Figure 10. Free-drift trajectories of baseline long maneuver profile with small nav error, zoomed out

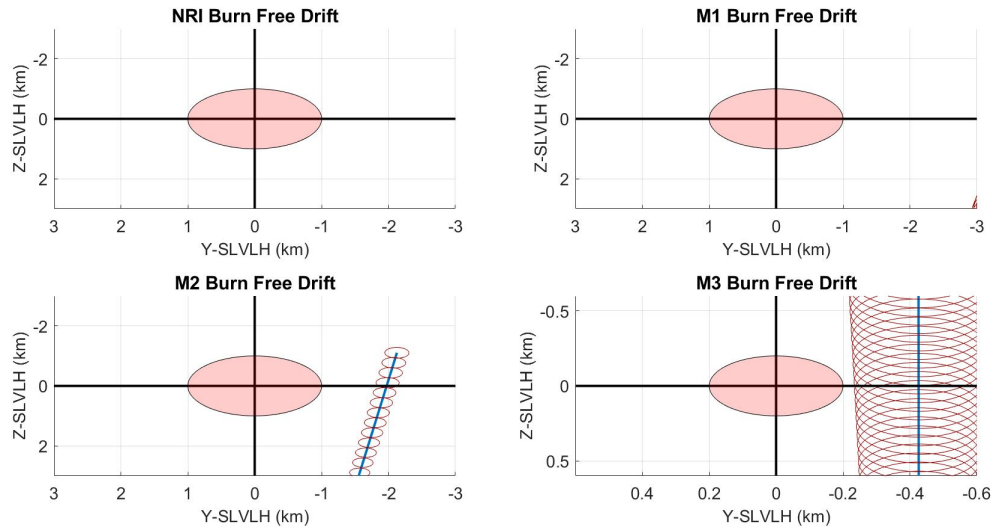


Figure 11. Free-drift trajectories of baseline long maneuver profile with small nav error, zoomed in

The trends seen with the large navigation error are exaggerated here, since the increased accuracy in state knowledge improves the targeting accuracy and thus reduces state dispersions over time. Once again, the profile is clearly unoptimized.

Case 1: Optimized Trajectory for Long Initiation Distance

Large Navigation Error Now optimizing the long case with large navigation error, the proposed maneuver profile meets all trajectory constraints with 19.857 m/s of total Δv usage between the HR1, HR2, and HR3 burns. Burn locations and ignition times are summarized in Table 3.

Table 3. Optimal maneuver profile for long initiation distance with large nav error

Burn	Location (km)	Ignition Time (sec)	Total ΔV (m/s)
NRI	$[0, 75, 225]^T$	0	-
HR1	$[0, 34.091, 141.49]^T$	7200	7.4540
HR2	$[0, 7.5031, 48.492]^T$	15400	3.5103
HR3	—	19000	8.8926

The maneuver profile with 3σ dispersions is presented in Figure 12 below. The shaded region is the 20° approach corridor about each side of the z-axis in the Sun-referenced LVLH coordinate frame.

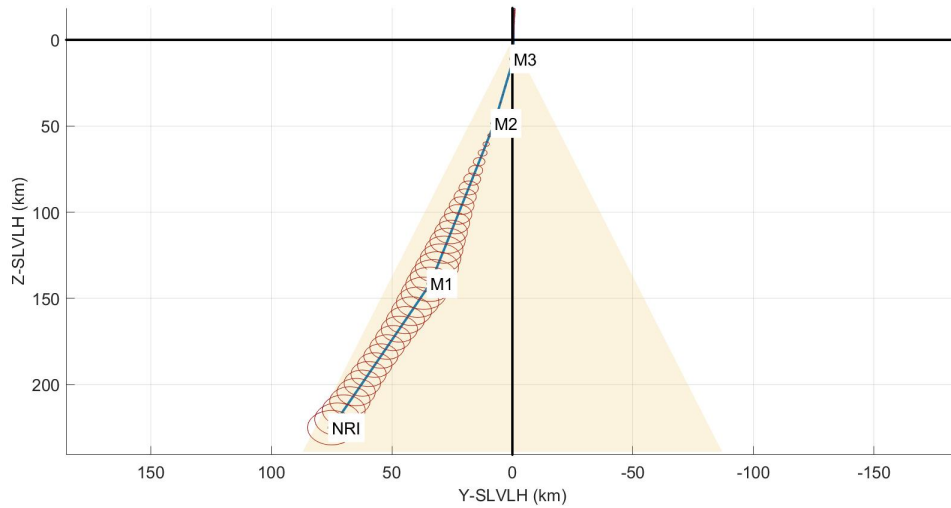


Figure 12. Optimal maneuver profile for long initiation distance with large nav error plotted in the Sun-referenced LVLH frame

Free drift profiles are presented in Figures 13 and 14 below. Note that although the ellipses may appear to violate the approach sphere constraint, the nominal trajectory has non-trivial x-components that ensure the spacecraft does not risk encroaching on the 3D sphere. Though the expectation is for all maneuvering to occur in the y-z plane, the optimizer has found an alternative approach for free drift trajectories thanks to the extra space from the NRI burn placement.

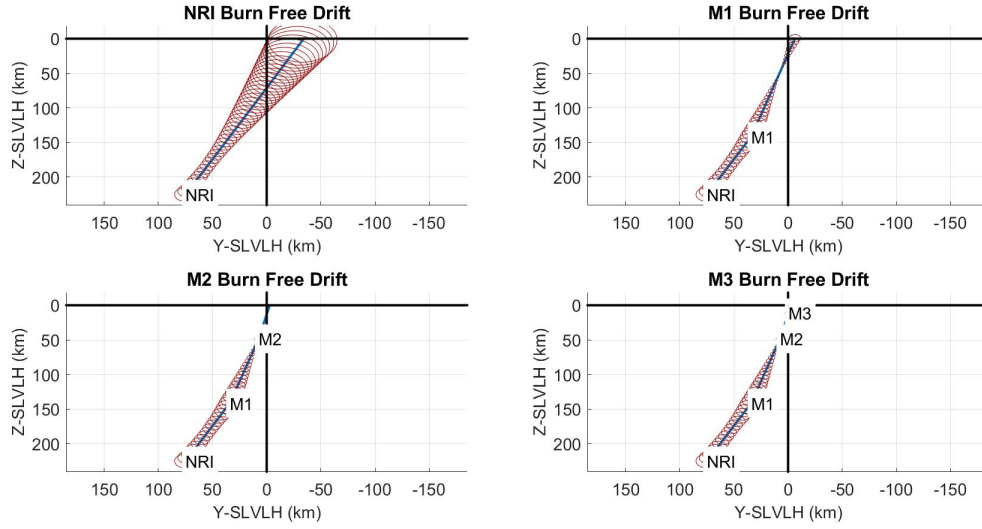


Figure 13. Free-drift trajectories of optimal long maneuver profile with large nav error, zoomed out

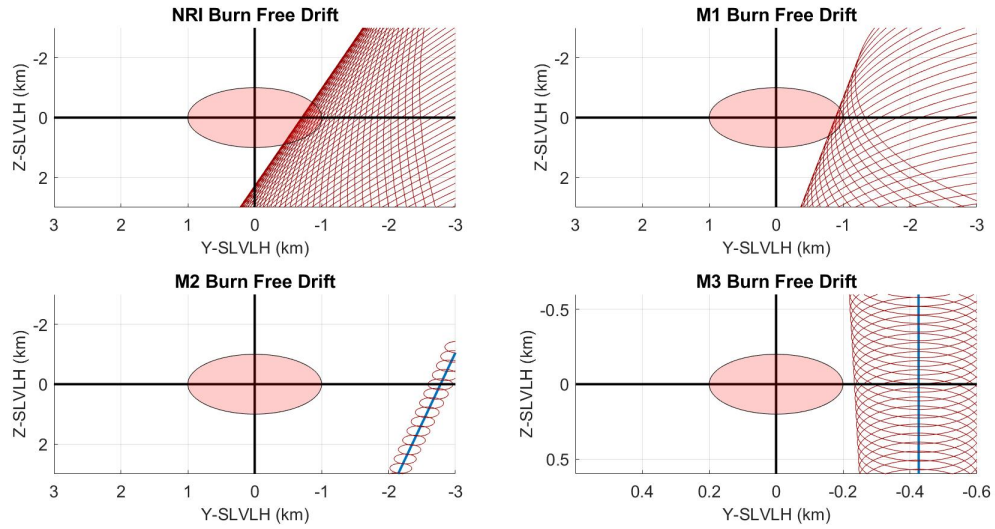


Figure 14. Free-drift trajectories of optimal long maneuver profile with large nav error, zoomed in

Small Navigation Error Next optimizing the long case with small navigation error, the proposed maneuver profile meets all trajectory constraints with 17.1794 m/s of total Δv usage between the HR1, HR2, and HR3 burns. Burn locations and ignition times are summarized in Table 4.

Table 4. Optimal maneuver profile for long initiation distance with small nav error

Burn	Location (km)	Ignition Time (sec)	Total ΔV (m/s)
NRI	$[0, 75, 225]^T$	0	-
HR1	$[0, 35.432, 137.37]^T$	7530	5.6866
HR2	$[0, 9.5271, 49.611]^T$	15390	2.1837
HR3	–	19000	9.3090

The maneuver profile with 3σ dispersions is presented in Figure 15 below. The shaded region is the 20° approach corridor about each side of the z-axis in the Sun-referenced LVLH coordinate frame.

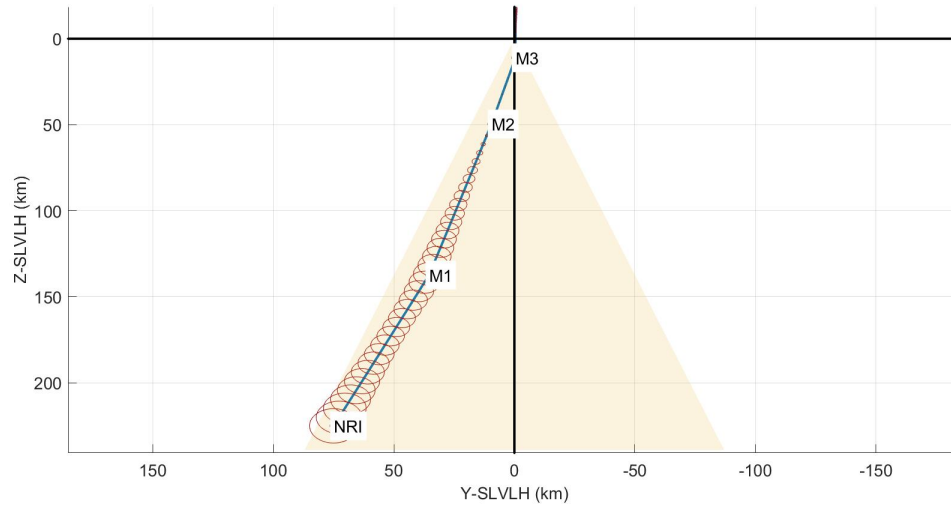


Figure 15. Optimal maneuver profile for long initiation distance with small nav error plotted in the Sun-referenced LVLH frame

Free drift profiles are presented in Figures 16 and 17 below.

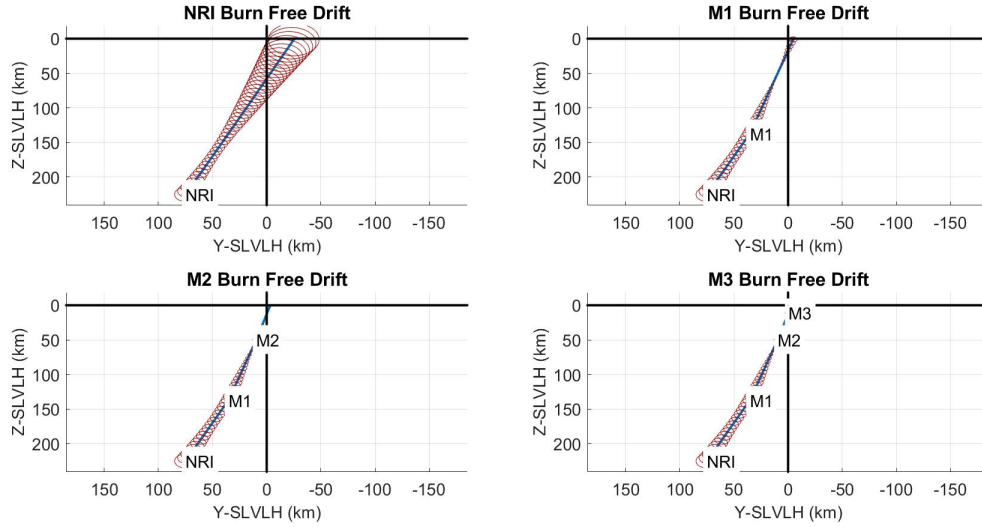


Figure 16. Free-drift trajectories of optimal long maneuver profile with small nav error, zoomed out

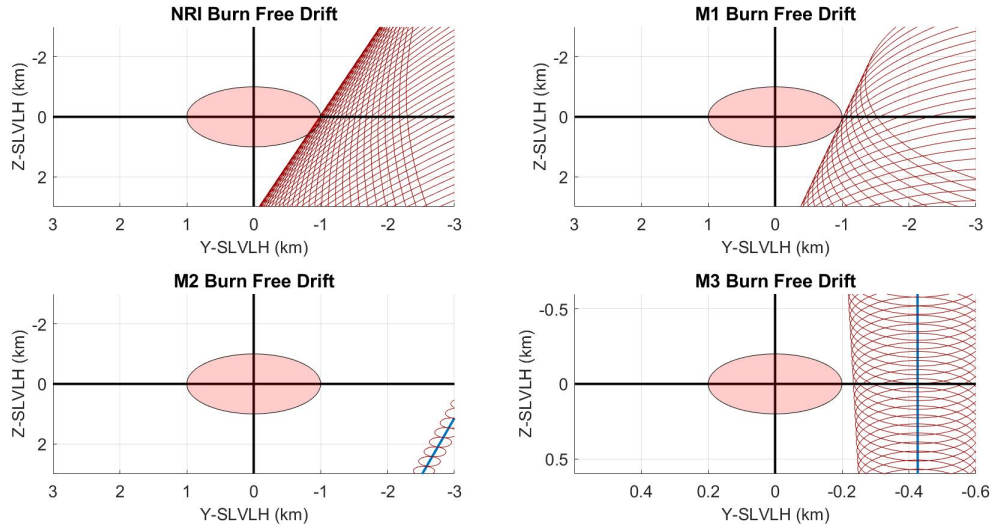


Figure 17. Free-drift trajectories of optimal long maneuver profile with small nav error, zoomed in

Unlike the previous case, the optimizer did not rely on out-of-plane free drifts to meet the constraint in this scenario. Though there may be some slight overlap between the 3σ position ellipses and the approach sphere in the y-z plane for the NRI burn free drift, it is far less significant than the optimized trajectory for the large navigation error.

Case 2: Optimized Trajectory for Medium Initiation Distance

Large Navigation Error Next optimizing the medium case with large navigation error, the proposed maneuver profile meets all trajectory constraints with 17.4878 m/s of total ΔV usage between the HR1, HR2, and HR3 burns. Burn locations and ignition times are summarized in Table 5.

Table 5. Optimal maneuver profile for medium initiation distance with large nav error

Burn	Location (km)	Ignition Time (sec)	Total ΔV (m/s)
NRI	$[0, 50, 175]^T$	0	-
HR1	$[0, 20.219, 116.00]^T$	6510	7.8123
HR2	$[0, 3.2771, 44.981]^T$	14625	3.6596
HR3	–	19000	6.0159

The maneuver profile with 3σ dispersions is presented in Figure 18 below. The shaded region is the 20° approach corridor about each side of the z-axis in the Sun-referenced LVLH coordinate frame.

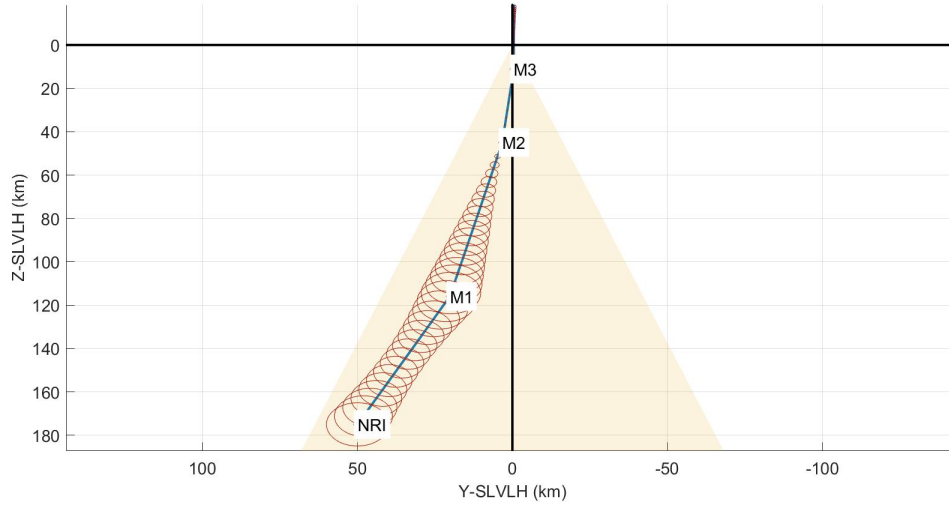


Figure 18. Optimal maneuver profile for medium initiation distance with large nav error plotted in the Sun-referenced LVLH frame

Free drift profiles are presented in Figures 19 and 20 below.

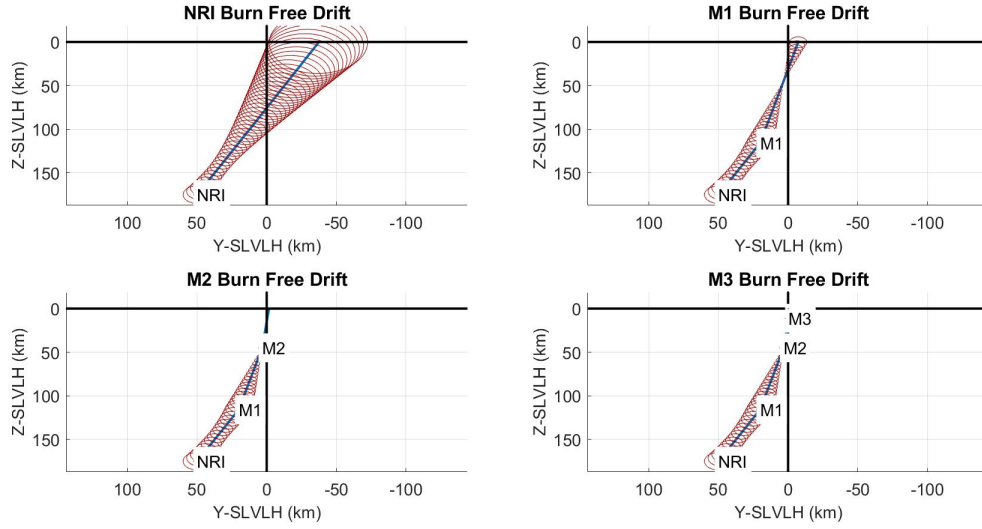


Figure 19. Free-drift trajectories of optimal medium maneuver profile with large nav error, zoomed out

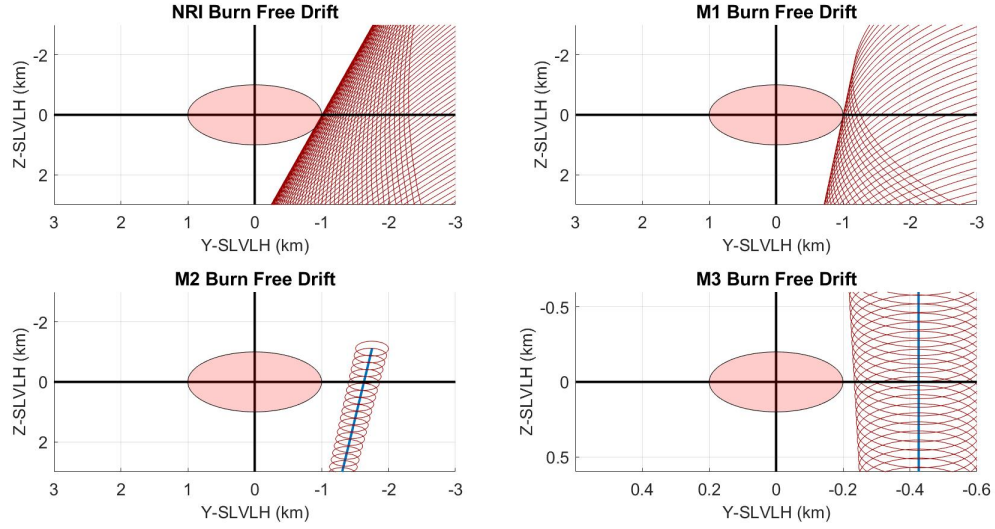


Figure 20. Free-drift trajectories of optimal medium maneuver profile with large nav error, zoomed in

The results shown here are fairly similar to those presented for the long initiation distance with small navigation error. No significant out-of-plane free drift motion is required to meet safety constraints.

Small Navigation Error Re-optimizing with a reduced initial navigation error, the proposed maneuver profile meets all trajectory constraints with 16.6839 m/s of total ΔV usage between the HR1, HR2, and HR3 burns. Burn locations and ignition times are summarized in Table 6.

Table 6. Optimal maneuver profile for medium initiation distance with small nav error

Burn	Location (km)	Ignition Time (sec)	Total ΔV (m/s)
NRI	$[0, 50, 175]^T$	0	-
HR1	$[0, 19.841, 104.62]^T$	7530	6.1619
HR2	$[0, 7.8296, 66.599]^T$	11940	4.3277
HR3	–	19000	6.1942

The maneuver profile with 3σ dispersions is presented in Figure 21 below. The shaded region is the 20° approach corridor about each side of the z-axis in the Sun-referenced LVLH coordinate frame.

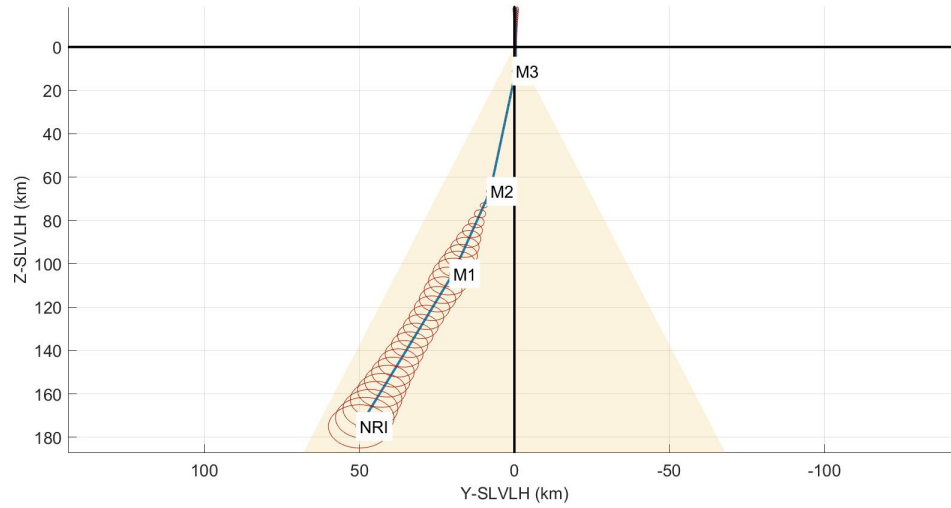


Figure 21. Optimal maneuver profile for medium initiation distance with small nav error plotted in the Sun-referenced LVLH frame

Free drift profiles are presented in Figures 22 and 23 below.

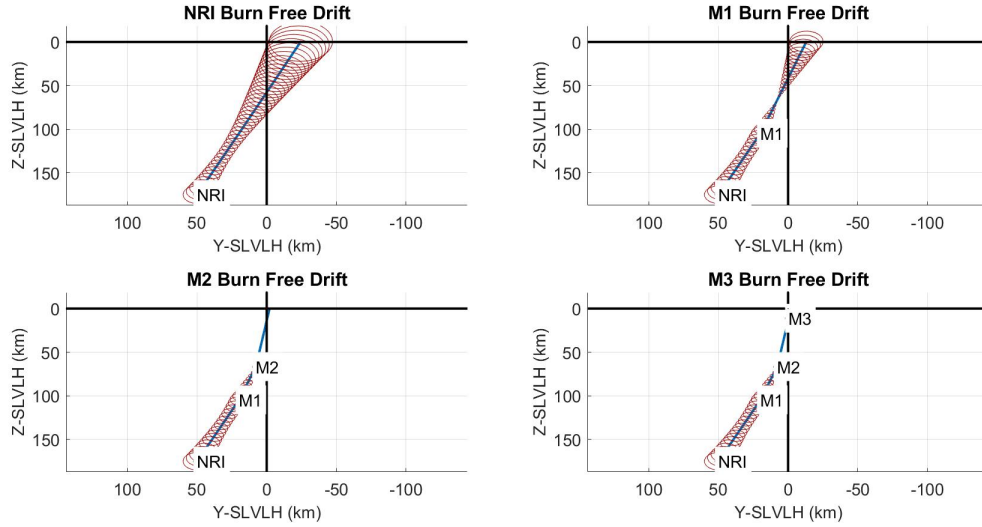


Figure 22. Free-drift trajectories of optimal medium maneuver profile with small nav error, zoomed out

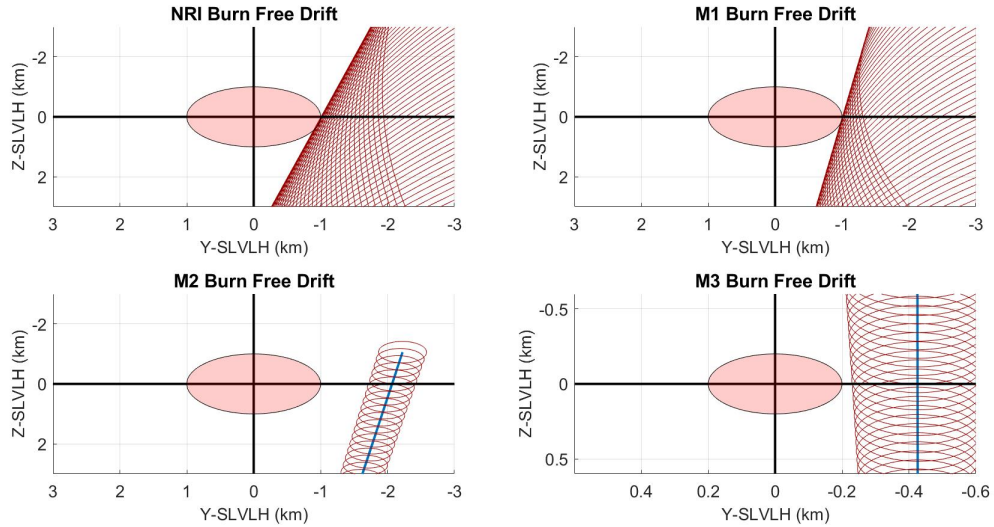


Figure 23. Free-drift trajectories of optimal medium maneuver profile with small nav error, zoomed in

The results appear fairly similar to the previous case. With the reduction in initial navigation error, maneuvers are more accurate and thus state dispersions grow slower over time, which in turn allows more direct routes to the target vehicle.

Case 3: Optimized Trajectory for Short Initiation Distance

Large Navigation Error Moving onto the short case with large navigation error, the proposed maneuver profile fails to meet the underburn safety constraint for the M2 burn. The profile meets all other constraints with 14.6879 m/s of total ΔV usage between the HR1, HR2, and HR3 burns. Burn locations and ignition times are summarized in Table 7.

Table 7. Optimal maneuver profile for short initiation distance with large nav error

Burn	Location (km)	Ignition Time (sec)	Total ΔV (m/s)
NRI	$[0, 25, 125]^T$	0	-
HR1	$[0, 4.0711, 82.796]^T$	6208.6	7.9743
HR2	$[0, -2.9202, 26.759]^T$	15390	4.1150
HR3	—	19000	2.6839

The maneuver profile with 3σ dispersions is presented in Figure 24 below. The shaded region is the 20° approach corridor about each side of the z-axis in the Sun-referenced LVLH coordinate frame.

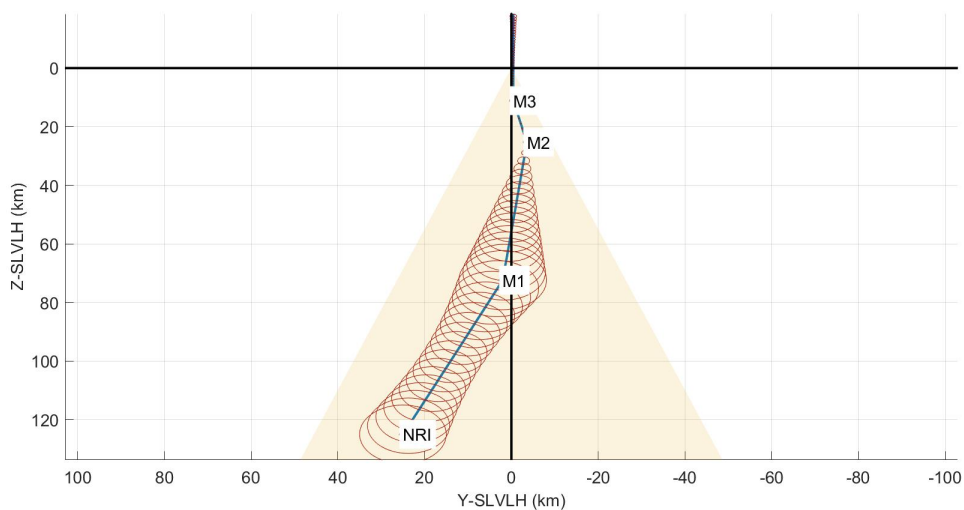


Figure 24. Optimal maneuver profile for short initiation distance with large navigation error plotted in the Sun-referenced LVLH frame

Free drift profiles are presented in Figures 25 and 26 below.

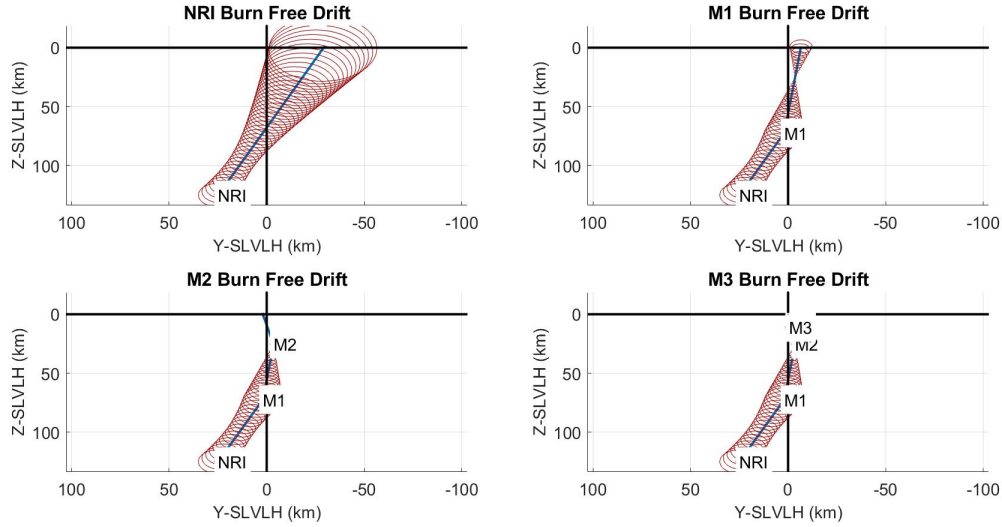


Figure 25. Free-drift trajectories of optimal short maneuver profile with large nav error, zoomed out

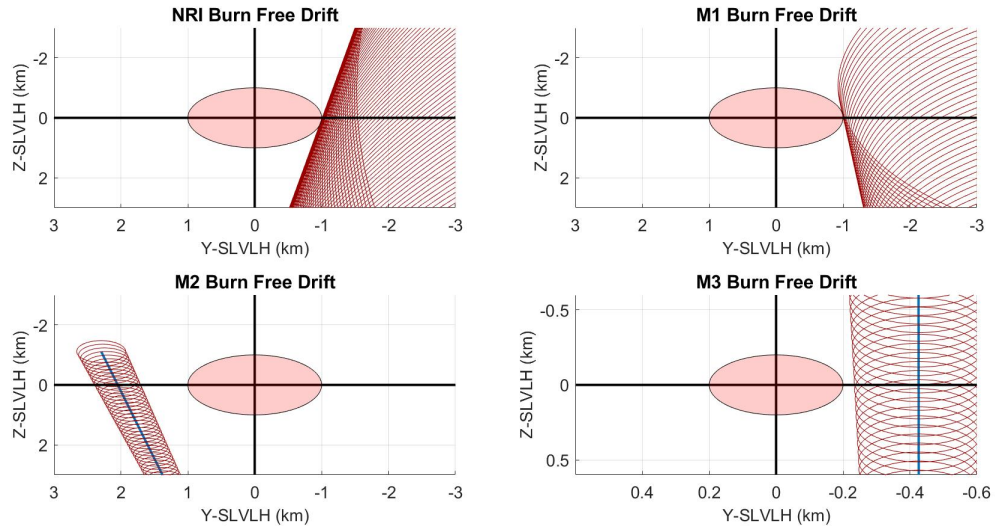


Figure 26. Free-drift trajectories of optimal short maneuver profile with large nav error, zoomed in

Despite numerous attempts at finding a satisfactory solution, the optimizers could not find a maneuver profile for the short initiation distance that met all safety constraints. This reflects the conflicting nature of the underburn and free drift constraints. The optimizer pushed the M2 burn location in the -y direction to meet the free drift constraint, but this in turn risks an underburn collision. Bringing the large initial state dispersions so close to the rendezvous point requires additional motion to try and meet all constraints, and with the requirement for two midcourse burns (M1 and M2) to be separated by at least an hour, there is simply not enough room to cut down on state dispersions in time. It is not unreasonable to suspect that eliminating the maneuver transfer time constraint or only conducting a single midcourse correction could produce a safe solution.

Small Navigation Error Finally examining the short case with small navigation error, the proposed maneuver profile fails to meet the free drift safety constraint for the NRI burn. The profile meets all other constraints with 12.0003 m/s of total ΔV usage between the HR1, HR2, and HR3 burns. Burn locations and ignition times are summarized in Table 8.

Table 8. Optimal maneuver profile for short initiation distance with small nav error

Burn	Location (km)	Ignition Time (sec)	Total ΔV (m/s)
NRI	$[0, 25, 125]^T$	0	-
HR1	$[0, 4.0711, 82.796]^T$	6208.6	7.9743
HR2	$[0, -2.9202, 26.759]^T$	15390	4.1150
HR3	-	19000	2.6839

The maneuver profile with 3σ dispersions is presented in Figure 27 below. The shaded region is the 20° approach corridor about each side of the z-axis in the Sun-referenced LVLH coordinate frame.

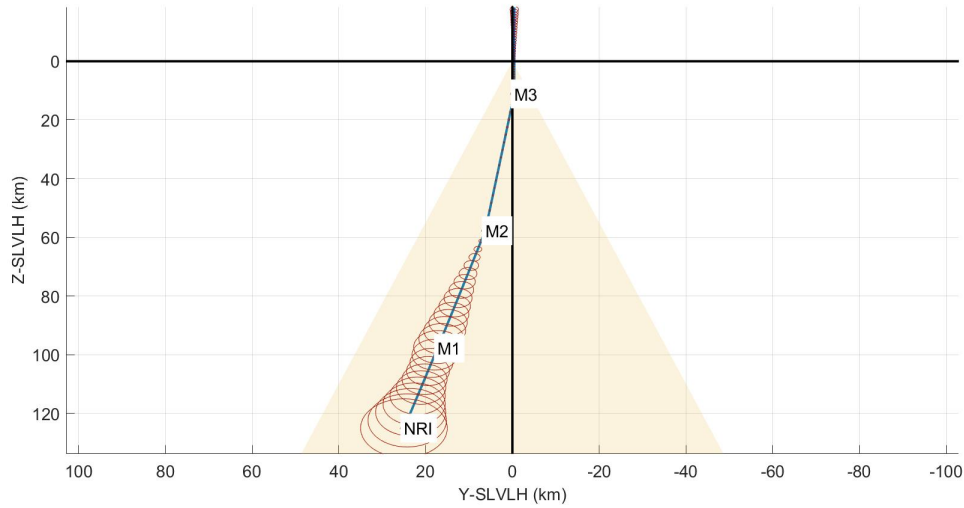


Figure 27. Optimal maneuver profile for short initiation distance with small navigation error plotted in the Sun-referenced LVLH frame

Free drift profiles are presented in Figures 28 and 29 below.

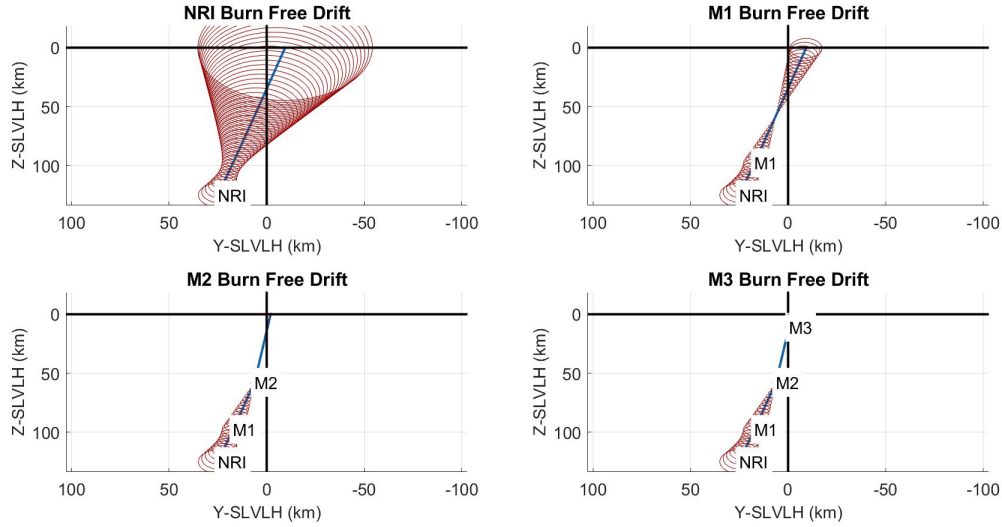


Figure 28. Free-drift trajectories of optimal short maneuver profile with small nav error, zoomed out

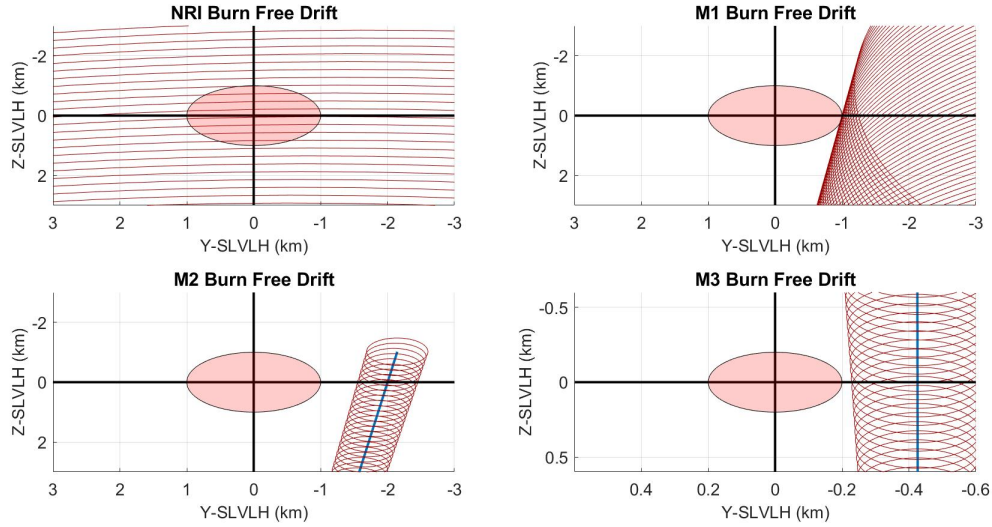


Figure 29. Free-drift trajectories of optimal short maneuver profile with small nav error, zoomed in

Once again, the conflicting underburn and free drift requirements required one to be violated. This time, it happened to be the free drift on the NRI burn. Though it is possible that a small enough navigation error could make this maneuver profile possible, it is more than likely necessary to eliminate the transfer time constraint or only conduct a single midcourse burn to meet all safety constraints.

CONCLUSION

The analysis presented in this paper demonstrates the application of robust trajectory optimization for rendezvous maneuver profile design in an NRHO. For long rendezvous initiation distances, out-of-plane motion proved useful for meeting safety constraints while permitting location targeting close to the target spacecraft. Medium initiation distances did not provide much more insight than this; however, the short

initiation distances demonstrated the practical limits of safe rendezvous when starting with significant state dispersions. If not enough distance is provided to conduct burns and reduce the state dispersions, one or more constraints will inevitably need to be broken. In all cases, reducing the initial navigation error reduced total Δv usage nontrivially, thus demonstrating the importance of an accurate navigation solution prior to conducting burns.

REFERENCES

- [1] J. Williams, D. E. Lee, R. J. Whitley, K. A. Bokelmann, D. C. Davis, and C. F. Berry, "Targeting Cislunar Near Rectilinear Halo Orbits for Human Space Exploration," *American Astronautical Society*, 1017, pp. AAS 17-267.
- [2] D. J. Grebow, M. T. Ozimek, K. C. Howell, and D. C. Folta, "Multibody Orbit Architectures for Lunar South Pole Coverage," *Journal of Spacecraft and Rockets*, Vol. 45, No. 2, March-April 2008.
- [3] K. Jin, D. K. Geller, and J. Luo, "Robust Trajectory Design for Rendezvous and Proximity Operations with Uncertainties," *Journal of Guidance, Control, and Dynamics*, Vol. 43, No. 4, 2020, pp. 741-753.
- [4] D. K. Geller, S. Shuster, D. Woffinden, and S. Bieniawski, "Robust Cislunar Trajectory Optimization via Midcourse Correction and Optical Navigation Scheduling," *44th Annual AAS Guidance, Navigation and Control Conference*, Breckenridge, CO, AAS 22-065, 4-9 February 2022 2022.
- [5] D. Woffinden, S. Shuster, and S. Geller, David Kand Bieniawski, "Robust Trajectory Optimization and GN&C Performance Analysis For NRHO Rendezvous," *2022 AAS/AIAA Astrodynamics Specialist Conference*, Charlotte, North Carolina, 22-564, 7-11 August 2022 2022.
- [6] G. Calkins, D. Woffinden, and Z. Putnam, "Robust Trajectory Optimization for Guided Powered Descent and Landing," *2022 AAS/AIAA Astrodynamics Specialist Conference*, Charlotte, NC, AAS 22-660, 7-11 August 2022 2022.
- [7] J. Joshi, D. Woffinden, and Z. Putnam, "End-to-End Mars Aerocapture Analysis Using Linear Covariance Techniques and Robust Trajectory Optimization," *2022 AAS/AIAA Astrodynamics Specialist Conference*, Charlotte, NC, AAS 22-678, 7-11 August 2022 2022.
- [8] S. GeShuster, "Development and Analysis of NRHO Rendezvous Reference Trajectories Using Convex Optimization," *42nd Annual AAS Guidance, Navigation and Control Conference*, Breckenridge, CO, AAS 19-014, 1-6 February 2019 2019.
- [9] P. S. Maybeck, *Stochastic models, estimation, and control*, Vol. 1. New York: Academic Press, 1979.
- [10] D. K. Geller, "Linear Covariance Techniques for Orbital Rendezvous Analysis and Autonomous On-board Mission Planning," *Journal of Guidance, Control, and Dynamics*, Vol. 29, November-December 2006, pp. 1404-1414.
- [11] T. J. Moesser and D. K. Geller, "Guidance and Navigation Linear Covariance Analysis for Lunar Powered Descent," *AAS/AIAA Astrodynamics Specialist Conference*, Mackinac Island, Michigan, AAS 07-313, 19-23 August 2007.
- [12] D. Geller and D. Christensen, "Linear Covariance Analysis for Powered Lunar Descent and Landing," *The Journal of Spacecraft and Rockets*, Vol. 46, Nov-Dec 2009, pp. 1231-1248.
- [13] D. Woffinden, S. Robinson, J. Williams, and Z. Putnam, "Linear Covariance Analysis Techniques to Generate Navigation and Sensor Requirements for the Safe and Precise Landing - Integrated Capabilities Evolution (SPLICE) Project," *AIAA Scitech 2019 Forum*, San Diego, CA, AIAA 2019-0662, 7-11 January 2019 2019.
- [14] J. W. Williams, W. E. Brandenburg, D. C. Woffinden, and Z. R. Putnam, "Validation of Linear Covariance Techniques for Mars Entry, Descent, and Landing Guidance and Navigation Performance Analysis," *AIAA Scitech 2022 Forum*, 2022, 10.2514/6.2020-0597.